

# Comparison of crystal orientation mapping-based and image-based measurement of grain size and grain size distribution in a thin aluminum film

Xuan Liu<sup>a</sup>, Andrew P. Warren<sup>b</sup>, Noel T. Nuhfer<sup>a</sup>, Anthony D. Rollett<sup>a</sup>,  
Kevin R. Coffey<sup>b</sup>, Katayun Barmak<sup>c,\*</sup>

<sup>a</sup> Department of Materials Science and Engineering, Carnegie Mellon University, 5000 Forbes Avenue, Pittsburgh, PA 15213, USA

<sup>b</sup> Department of Materials Science and Engineering, University of Central Florida, 4000 Central Florida Boulevard, Orlando, FL, USA

<sup>c</sup> Department of Applied Physics and Applied Mathematics, Columbia University, 500 W. 120th St., New York, NY 10027, USA

Received 27 May 2014; received in revised form 4 July 2014; accepted 6 July 2014

Available online 8 August 2014

## Abstract

Crystal orientation maps of a nanocrystalline Al film were obtained using precession electron diffraction in a transmission electron microscope. The orientation maps were then subjected to a series of well-defined clean-up procedures for removal of badly indexed points and pseudosymmetry boundaries. The mean grain size and grain size distribution were obtained from the reconstructed boundary network. The grain size and grain size distribution were also measured by the conventional transmission electron microscopy bright-field-imaging-based hand-tracing methodology, and were compared quantitatively with the orientation mapping results. It was found that the mean grain size from the two methodologies agree within experimental error. On the other hand, the orientation mapping methodology produced a somewhat different grain size distribution compared with the distribution obtained by the hand-tracing methodology. The reasons for the differences in the distributions are discussed.

© 2014 Acta Materialia Inc. Published by Elsevier Ltd. All rights reserved.

**Keywords:** Transmission electron microscopy (TEM); Crystallographic orientation; Nanocrystalline aluminum; Grain size; Thin film

## 1. Introduction

It is well known that the grain structure of nanocrystalline thin films has a strong influence on film properties [1–4]. Therefore, the establishment of quantitative structure–property relations is of great scientific and technological interest. In order to develop quantitative structure–property relations, quantitative measures of the grain structure, such as the mean grain size and the grain size distribution, are required. Quantitative measures of

grain structure are also critical for comparisons with predictions of grain growth simulations and models, and for the development of grain growth theories.

Barmak et al. [5] recently reported a detailed quantitative comparison of the grain structure of Cu and Al films with two-dimensional grain growth simulations. The experimental dataset was large and included the grain size of more than 30,000 grains from 25 films. The size distributions for Al and Cu were found to be remarkably similar to each other despite the many and significant differences in experimental conditions, which included sputtering target purity, substrate type, film thickness, deposition temperature, actual as well as homologous annealing temperatures, annealing time, absolute grain size, and the twin

\* Corresponding author.

E-mail addresses: [xuanliu@andrew.cmu.edu](mailto:xuanliu@andrew.cmu.edu), [xuanliucmu@gmail.com](mailto:xuanliucmu@gmail.com) (X. Liu), [katayun.barmak@columbia.edu](mailto:katayun.barmak@columbia.edu) (K. Barmak).

density within the grains. This similarity argued for a universal grain size distribution, which for grain diameters is log-normal as found previously for thin films. In a recent work, large-scale numerical simulations were used to examine the phenomenon of grain growth in two-dimensional systems [6]. The simulation results were in good agreement with the universal grain size distribution determined by Barmak et al. [5,6]. However, much, though not all, of the experimental data in Barmak et al.'s study was obtained by hand tracing of transmission electron microscopy (TEM) images obtained by bright-field, hollow cone dark-field scanning, and conical dark-field techniques. Given the painstaking and slow nature of hand tracing, it would appear interesting to see if automated boundary tracing methods can be used to obtain the grain size and grain size distribution. One such automated tracing method is the reconstruction of the boundary network in crystal orientation maps, wherein grain boundaries are located by the misorientation of adjacent points. Crystal orientation maps of nanocrystalline materials using precession-assisted electron diffraction [7–16] in a transmission electron microscope can now be obtained with relative ease, allowing ready access to the reconstructed boundary network amenable to quantification of grain size and grain size distribution.

The aim of the current paper is to report an automated methodology for grain size measurement of nanocrystalline materials based on TEM crystal orientation mapping. The sample used for the study is an Al thin film. The grain size and grain size distribution of the Al thin film were measured by both the automated methodology and the traditional hand-tracing methodology to allow comparison of the two methods.

## 2. Experiments

### 2.1. Film deposition and TEM sample preparation

The Al sample examined in this work has a nominal thickness of 100 nm. It was sputter-deposited at room temperature and was post-deposition annealed at 400°C in Ar + 4% H<sub>2</sub> for 2.5 h. The plan-view TEM sample was prepared by first removing most of the Si by mechanical polishing from the back side. Chemical etching with a mixture of HF and HNO<sub>3</sub> was then used for further thinning [17]. The etching was stopped before breaking into the Al film, resulting in a large, uniformly thick, electron-transparent sample for TEM.

### 2.2. Orientation mapping for data collection

All of the orientation maps were recorded using an ASTAR<sup>TM</sup> (NanoMEGAS, Brussels, Belgium) orientation mapping system installed on a FEI Tecnai F20 transmission electron microscope (FEI Corporation, Hillsboro, OR) with a field emission gun and an accelerating voltage of 200 kV. Diffraction patterns were recorded with a

precession angle in the range of 0.7°–1° and a step size of 5 nm. A detailed description of the orientation mapping system can be found in earlier publications [7–9,18–20]. Diffraction patterns are acquired as the beam is scanned over the area of interest. Precession was used to reduce the dynamic effect, making the patterns easier to index [8,10,21]. This precession-enhanced crystal-mapping technique has recently been used to measure the grain boundary character distributions in nanocrystalline Cu and W films [11,12,15], as well as the heterophase interfacial characters in nanolamellar Cu/Nb composites [13,14,16]. The orientation maps were analyzed using TSL OIM<sup>TM</sup> software (EDAX, Mahwah, NJ) after adjusting for the reference frame difference between the ASTAR<sup>TM</sup> and TSL systems, as described in detail elsewhere [11,14]. For the current study, a counterclockwise rotation of 207° was used to bring the diffraction pattern and image into coincidence.

### 2.3. Data clean-up for grain size measurement

The raw orientation mapping data was subjected to a clean-up procedure to eliminate incorrectly indexed data points. The clean-up influences the grain size measurement result and is therefore defined in a systematic manner. The first clean-up step is grain dilation, which has two specific parameters: the minimum grain size and the misorientation tolerance angle. The misorientation tolerance angle, below which two pixels are considered to belong to the same grain, is assumed to be 5°. The minimum grain size, on the other hand, was taken as 5% of the average grain area calculated from raw orientation maps. Here, we choose 5% of the average grain area since very few grains in the reported universal grain size distribution [5] have values < 5% of the mean. For the Al sample studied here, raw orientation maps give an average grain area of 3509 nm<sup>2</sup>. 5% of this grain area is 175 nm<sup>2</sup>. This corresponds to a minimum grain size of  $175/(5 \times 5) = 7$  pixels, where 5 corresponds to the lateral and vertical step size in nm. Next, a single, averaged orientation was assigned to all of the pixels within a grain, assuming all adjacent pixels with misorientations < 5° belonged to the same grain. Finally, the pseudosymmetry clean-up was used to remove false boundaries that are created within single grains when patterns can be indexed in multiple orientations related by simple symmetry operations [12]. Here, a total of 21 types of pseudosymmetry boundaries, including 60°/⟨111⟩, were identified and removed based on the misorientation between pixels on the two sides of the pseudosymmetry boundary. The misorientation axis and angle as well as the percentage of data points changed for the 21 pseudosymmetry boundary types are listed in Table 1. False 60°/⟨111⟩ boundaries were removed with a tolerance of 2°, whereas false 180° boundaries were removed with a tolerance of 1°. Approximately 4% of the data points were changed during the pseudosymmetry clean-up procedure. Grain boundary line segments were then reconstructed on the orientation maps with deviation from the true

Table 1.

Misorientation angle, axis, as well as percentage of data changed for each pseudosymmetry boundary that was removed during the clean-up procedure.

Angle	Axis	% Of data changed
60	111	1.7
180	001	0.02
180	101	0.04
180	102	0.2
180	103	0.3
180	104	0.03
180	105	0.02
180	113	0.7
180	114	0.02
180	116	0.2
180	117	0.03
180	212	0.02
180	213	0.05
180	215	0.04
180	223	0.05
180	313	0.5
180	314	0.02
180	315	0.05
180	317	0.05
180	323	0.04
180	525	0.03

boundary positions of no more than two pixels. A sample orientation map overlaid with reconstructed boundary network before and after pseudosymmetry boundary clean-up can be found in Fig. 1a and b. The reconstructed boundary network from ~40 fields of views was used for grain size measurement. The edge grains in each field of view were excluded from measurement.

#### 2.4. Bright-field-imaging-based hand-tracing for grain size measurement

Hand-tracing of conventional bright-field images was also used to measure the grain size of the same Al film. Nine fields of views were collected. For each field of view, four or five bright-field images were taken at different sample tilts ranging from approximately  $-4^\circ$  to approximately  $4^\circ$ . Grain boundaries were traced by hand onto a transparency, which was then scanned to create a digital image. In Fig. 2, bright-field images at five different sample tilts are shown, together with the hand-traced grain boundary network.

#### 2.5. Grain size determination

The mean grain size in this work is defined as the equivalent circle diameter of the mean area. The mean area  $\bar{A}$  is calculated based on areas of individual grains:

$$\bar{A} = \left(\frac{1}{n}\right) \sum_i A_i \quad (1)$$

The equivalent circle diameter of the mean area is defined as:

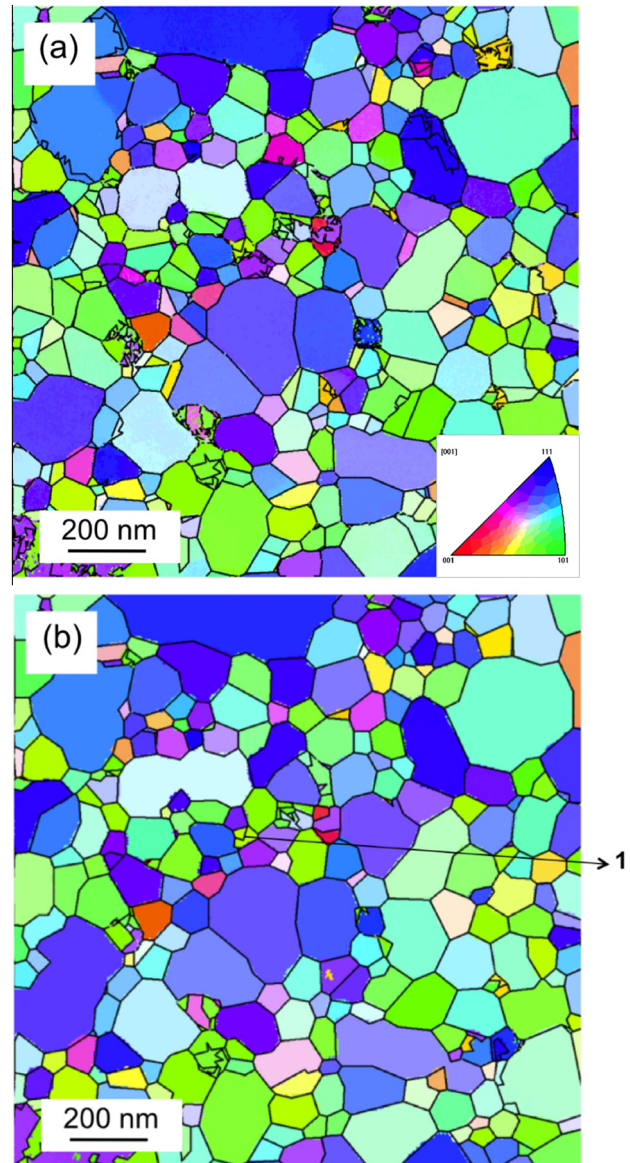


Fig. 1. Representative inverse pole figure map of the Al thin film in the sample normal direction with superimposed reconstructed grain boundary line segments (black lines) (a) before and (b) after removal of pseudosymmetry boundaries. The surface normals of the grains are colored by orientation according to the inset key. In (b) the boundary marked “1” is a pseudosymmetry boundary. See text for more detail. (For interpretation of the references to colour in this figure legend, the reader is referred to the web version of this article.)

$$D_A = \sqrt{\frac{4\bar{A}}{\pi}} \quad (2)$$

#### 2.6. Grain size distribution and the Hellinger distance

The distribution of grain sizes in thin films follows a log-normal probability density [5,22,23]. The probability density  $f(x)$  of the lognormal distribution is given by:

$$f(x) = \frac{1}{x\sigma\sqrt{2\pi}} \times \exp\left(\frac{-(\ln x - \mu)^2}{2\sigma^2}\right), \quad (3)$$

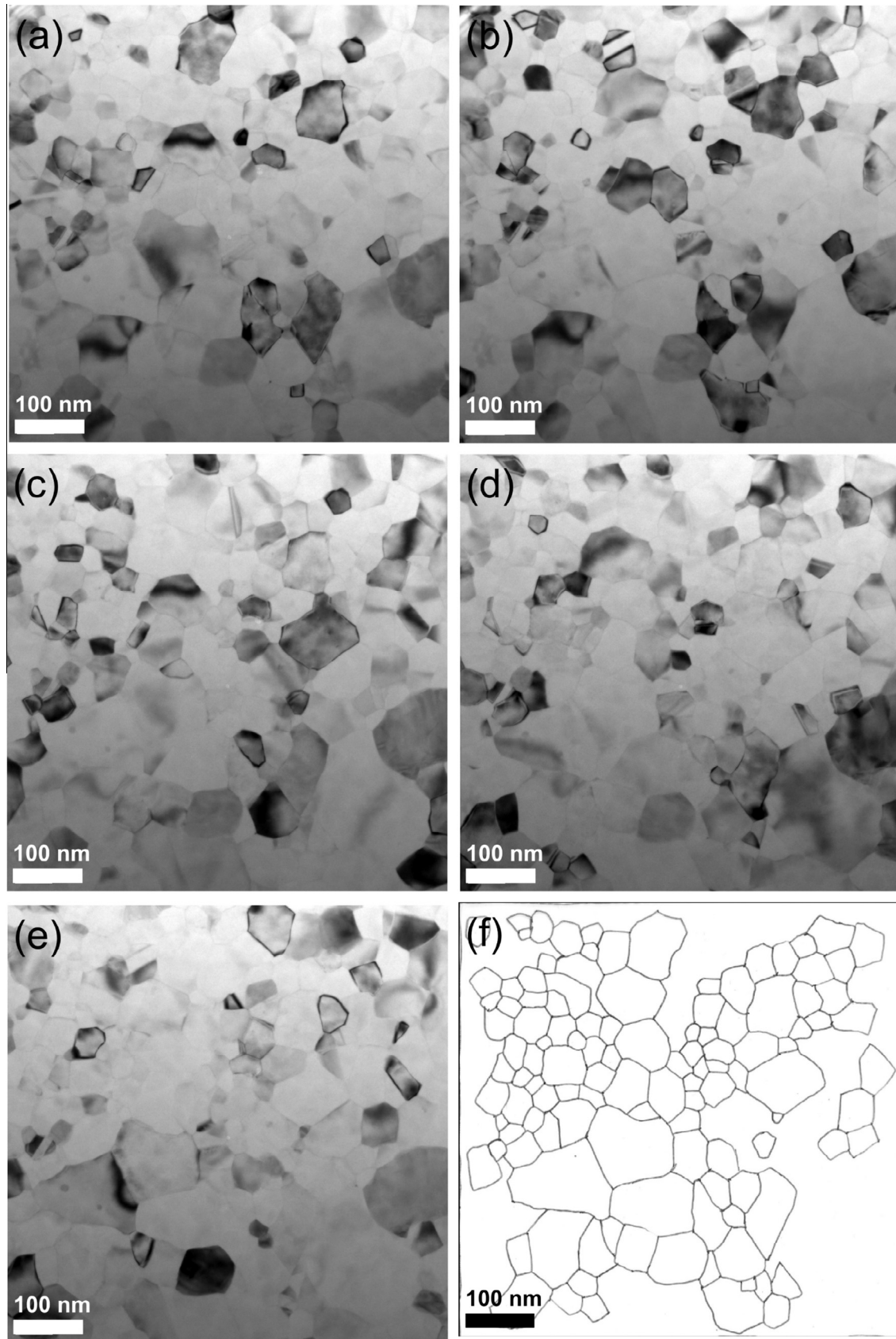


Fig. 2. Representative bright-field TEM images of a field of view taken at sample tilt angles of (a)  $-3.5^\circ$ , (b)  $-1.7^\circ$ , (c)  $0.9^\circ$ , (d)  $2.8^\circ$  and (e)  $3.9^\circ$ ; (f) the grain boundary network traced by hand using images (a)–(e). Note that the contrast between grains varies rapidly with tilt angle, thereby allowing nearly all the grains to be identified.



where  $\sigma$  and  $\mu$  are independent fitting parameters.

For a quantitative measure of how closely the distributions from the two methods compare with each other, use was made of a measure of the “distance between distributions”. In this work, the similarity of the distributions was quantified by the modified Bhattacharyya coefficient  $H(p, q)$ , which is also known as the Hellinger distance [24]. The Hellinger distance has been found to provide a balance between the ease of use and the ability to distinguish between two different density maps  $p$  and  $q$  [25,26]. The regular Bhattacharyya coefficient  $\beta(p, q)$  is a measure of the similarity between two normalized distributions [24,25] and can be written in the following form:

$$\beta(p, q) = \sum_{i=1}^N \sqrt{p(i)q(i)} \left( \text{with } \sum_{i=1}^N P(i) = \sum_{i=1}^N q(i) = 1 \right) \quad (4)$$

The Hellinger distance  $H(p, q)$  is defined by:

$$H(p, q) = \sqrt{1 - \beta(p, q)} \quad (5)$$

The smaller the Hellinger distance, the more similar the two distributions are. Two identical distributions have a Hellinger distance of 0.

Compared with histograms, the traditional representations of grain size distributions, probability plots are useful, both for showing correlation of sample distributions to theoretical distributions on a linearized basis and for examination of the tails of the distributions (for grain sizes  $\gg$  mean grain size), known as the extreme values [27,28]. In the probability plot, the logarithms of the grain radii,  $R$ , are normalized by their mean, i.e.  $\log(R/\langle R \rangle)$ . Therefore, grain size data that follow a log-normal distribution will conform to a line [27].

### 3. Results and discussion

#### 3.1. Grain size measurement

Grain size measurement results using the ASTAR<sup>TM</sup> orientation mapping methodology as well as the bright-field-imaging-based hand-tracing methodology are listed in Table 2. Grain size values are given as the equivalent circle diameter of the mean area and are calculated as  $94 \pm 4$  and  $96 \pm 5$  nm with 2363 and 1138 grains measured, respectively, using the two methodologies. The errors on these diameters are quoted as  $\pm$  one-half of the confidence interval at a confidence level of 95% for the given population [29]. The two methods give the same grain size value

when the confidence interval is taken into account. However, the orientation mapping-based grain size measurement method requires much less human and time input since all procedures are nearly fully automated.

#### 3.2. Grain size distribution

Histograms of the grain size distributions obtained from the two methodologies, i.e. TEM bright-field-imaging-based hand-tracing and TEM orientation mapping, are plotted in Fig. 3a and b, respectively. The grain size data were fit to the log-normal distribution function (Eq. (3)), as shown in the figure. The probability plots of the image-based distribution, the orientation mapping-based distribution and the universal distribution are given in Fig. 4.

Examination of the grain size distributions in Fig. 3 reveals that the orientation mapping data shown in Fig. 3b has a larger fraction of grains on the small side of the distribution compared to the image-based distribution.

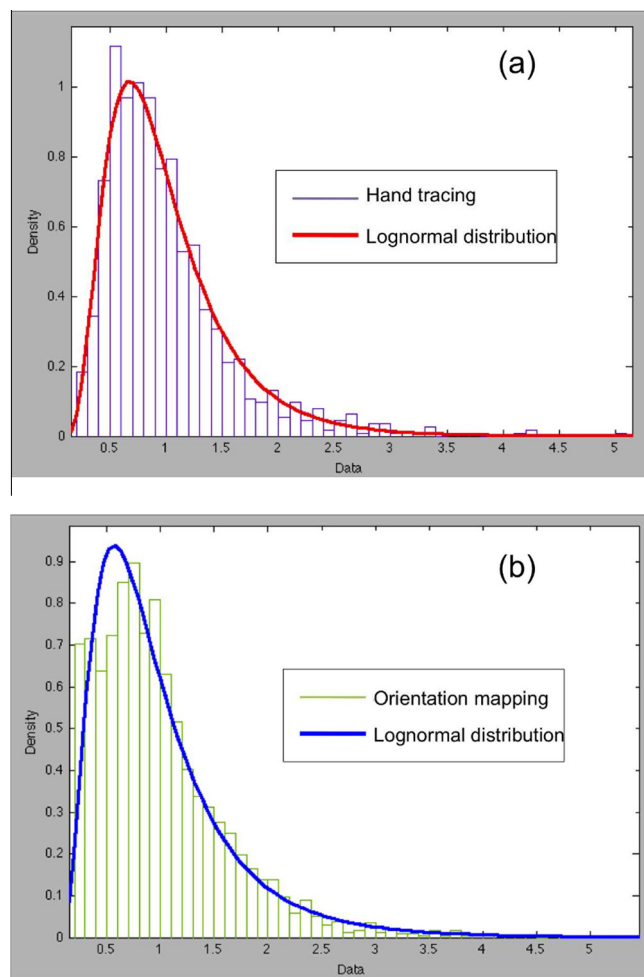


Fig. 3. Grain size distribution for (a) hand-tracing data based on TEM bright-field micrographs and (b) TEM crystal orientation mapping data. Both data were fitted with a log-normal probability density function. The fitting parameters are given in Table 3.

Table 2.

Grain size measurement results for the annealed Al film using a crystal-orientation mapping-based automated method and a bright-field-imaging-based hand-tracing method.

	Grain size (nm)	No. of grains measured
TEM crystal orientation mapping	$94 \pm 4$	2363
Bright-field imaging	$96 \pm 5$	1138

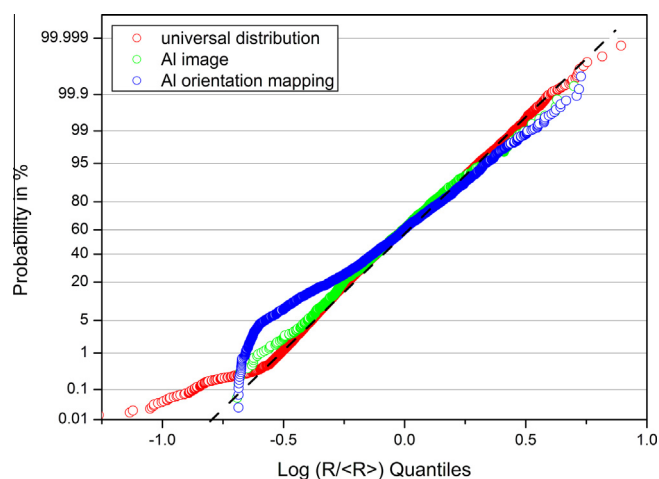


Fig. 4. Probability plot of the image-based AI data, the orientation mapping-based AI data and the universal data.  $R$  and  $\langle R \rangle$  are the circle equivalent radius and the mean of the grain radii, respectively.

This increase in the fraction of small grains is likely a result of the inability to remove all pseudosymmetry boundaries. The reasons for the differences between the two distributions will be presented later in this section. The probability plots shown in Fig. 4 give similar results. The deviation of the orientation mapping data from the log-normal distribution (represented by the dashed line) is greater than that of the other two datasets. The deviation is particularly obvious for grain sizes smaller than the mean ( $\log(R/\langle R \rangle) < 0$ ), evidenced by the hump in the curve as compared with the dashed line, which represents the log-normal distribution [27].

The ratio of the median-to-mean grain size, i.e.  $D_{med}/\langle D \rangle$ , can also be used to evaluate the similarity of grain size distributions. For the current AI dataset, the ratio obtained by the hand-tracing methodology is 0.87. For the orientation mapping methodology, on the other hand, the ratio is 0.84. The fitting parameters  $\sigma$  and  $\mu$ , as well as the median-to-mean ratio for the two distributions, are given in Table 3. The median-to-mean ratio of 0.87 for the hand-tracing methodology compares well with the value of 0.89 reported for the universal grain size distribution, for which the individual data sets when considered separately gave ratios of  $0.87 \pm 0.03$ .

The Hellinger distance between the orientation mapping distribution and the hand-tracing distribution is calculated to be 0.02203 using Eqs. (4) and (5). For a better understanding of this Hellinger distance, two groups of grains, with 1000 grains in each group, were selected from the

more than 30,000 grains in the universal distribution and the Hellinger distance between the two groups was calculated. The procedure was repeated 5, 20, 50, 100, 200 and 500 times. Values of the average Hellinger distance as well as the standard deviation with each repetition time are shown in Table 4. The average Hellinger distance as well as the standard deviation reached a plateau at  $\geq 100$  repetitions. As a result, if two distributions have a Hellinger distance smaller than  $0.01320 + 0.0039 = 0.0171$ , then they are considered to belong to the same distribution. Compared with this value, the orientation mapping distribution and the hand-tracing distribution has a Hellinger distance  $> 0.0171$ . Therefore, the orientation mapping-based methodology gives a different distribution compared with the hand-tracing methodology.

The reason for the difference in the grain size distribution between the two methodologies is likely the result of artifacts in orientation mapping. To generate the orientation maps, the orientation of each scanned point is determined via cross-correlation between the collected diffraction pattern and pre-calculated templates. The quality of orientation mapping is therefore strongly dependent on the quality of diffraction patterns, as well as on artifacts caused by the procedure by which the orientation is assigned. These artifacts are discussed below:

1. The diffraction pattern is not on the zone axis: for grains not oriented along the zone axis, only a few reflections in reciprocal space can be excited. Precession is used to alleviate this problem. Using precession, the incident beam is tilted, in most cases,  $0.1^\circ$ – $1^\circ$  from the optical axis, and is rocked through the Bragg condition. Dynamic effects can be greatly reduced using precession and diffraction is closer to the kinematic condition, resulting in significantly more diffraction spots in the diffraction pattern and consequently greater reliability of indexing via template matching. However, the precession angle may not be large enough and the point may be assigned an incorrect orientation. It must be noted that the analysis software of the ASTAR<sup>TM</sup> system always assigns an orientation to a given diffraction pattern no matter how few the number of diffraction spots, even though the reliability of the assignment is low.
2. Sample artifacts including, for example, contamination and voiding, which can result in incorrect orientation assignment to a given point. In addition, in regions close

Table 3.

The fitting parameters  $\sigma$  and  $\mu$  of the log-normal distribution as well as the median to mean ratio of the grain size distribution obtained by hand-tracing and orientation mapping.

	$\sigma$	$\mu$	Median-to-mean ratio
Hand-tracing	0.51	−0.14	0.87
Orientation mapping	0.62	−0.18	0.84

Table 4.

The average Hellinger distance and standard deviation with different repetition times.

No. of repetitions	Average Hellinger distance	Standard deviation
5	0.0158	0.0071
20	0.0145	0.0042
50	0.0137	0.0042
100	0.0132	0.0040
200	0.0132	0.0038
500	0.0132	0.0039

to grain boundaries, the electron beam may overlap two grains, resulting in superimposed diffraction patterns and consequently incorrect orientation assignment for a given point.

Most badly indexed data points at grain boundaries and within grains resulting from the above two artifacts will be removed using the grain dilation step during data clean-up, as described in the experimental section. Therefore, these incorrectly indexed points are not expected to result in the observed differences in the grain size distributions, because the minimum grain size selected for the grain dilation step (5% of the mean grain area prior to clean-up) was chosen based on earlier grain size measurements incorporated in the universal distribution, which shows excellent agreement with the hand-tracing distribution obtained in this work. It is the third artifact in the orientation mapping that is expected to be the key reason for the difference in the hand-tracing and orientation mapping based grain size distributions, as detailed below.

3. Pseudosymmetry boundaries: the presence of pseudosymmetry boundaries in the orientation maps is caused by the fact that symmetrically related diffraction patterns, i.e. patterns related by rotations along certain axes, are identical and cannot be distinguished in spot diffraction patterns that are obtained using the ASTAR<sup>TM</sup> system. During template matching, two templates related by a pseudosymmetry relation may be randomly assigned to different orientations within the same grain, resulting in pseudosymmetry boundaries, which are false boundaries. Precession can help reduce the number of pseudosymmetry boundaries by exciting reflections from higher-order Laue zones [8], and the analysis software TSL OIM<sup>TM</sup> can be used to remove many of the remaining pseudosymmetry boundaries. The 21 pseudosymmetry boundaries commonly found in cubic materials are listed in Table 1.

The nanocrystalline Al film studied in this work represents a nearly ideal situation for the orientation mapping-based methodology: (i) the film has a moderate grain size of 94 nm; (ii) it has a simple microstructure that is not affected by contamination and is void-free; (iii) the TEM sample is well-prepared with large thin areas; (iv) a high precession angle of 0.7°–1° is used to excite reflections in higher-order Laue zones. However, the orientation maps are still affected by the pseudosymmetry issue as seen in Fig. 1a, despite the high precession angle. Some of these pseudosymmetry boundaries persist even after cleaning the 21 types of boundaries listed in Table 1. For example, the pseudosymmetry boundary marked by “1” in Fig. 1b deviates by only 2° from the 180°<104> boundary type as defined in Table 1. The reason why the tolerance angle of pseudosymmetry clean-up cannot be increased is that higher tolerance angles result in removal of a large number of real grain boundaries together with pseudosymmetry boundaries. Pseudosymmetry boundaries such as the one

marked in Fig. 1b can be individually removed based on the misorientation relation, but the procedure is not automated and will require an equally painstaking effort as used in hand-tracing to identify each misorientation relation and to remove the boundary. The pseudosymmetry boundaries that remain after the automated removal of the 21 types listed in Table 1 divide a grain into two or more smaller grains. Therefore, the number of grains with sizes just larger than the cut-off size defined in the grain dilation step is larger for the orientation mapping data than for the hand-tracing data, as shown in Fig. 3a and b.

In principle it is possible to reduce the number of pseudosymmetry boundaries even further by increasing the precession angle to the current system limit of 3°. However, the increase in precession angle will impose increasing difficulty in precession alignment. Moreover, the beam size will increase with increasing precession angle due to spherical aberration in the transmission electron microscope and will eventually influence the spatial resolution of the mapping. Therefore, the difference in the measured grain size distribution between the hand-tracing and orientation mapping methodologies resulting from the presence of pseudosymmetry boundaries is an intrinsic artifact of the orientation mapping system in its current form and requires improvements in the mapping system and in the analysis software.

In spite of the difference in the grain size distribution between the two methodologies, orientation mapping offers an extremely useful approach to metrology of nanocrystalline materials. It captures the average grain size accurately and can shorten the data acquisition time by 4/5 compared with the hand-tracing methodology. Moreover, it provides orientation information for each scanned point, which is beneficial for microstructural analysis of boundary types present in the sample [11,12]. If the value of the mean grain size is the only concern, then the automated orientation mapping-based grain size measurement can be considered to be of high accuracy and efficiency for nanocrystalline materials.

#### 4. Conclusions

The mean grain size and the grain size distribution of an annealed nanocrystalline Al film were obtained from the reconstructed boundary network in crystal orientation maps and from the hand-traced boundary network in conventional TEM bright-field images. The mean grain size from the two methods was found to agree within experimental error, and the grain size distributions were found to be well described by the log-normal distribution. The grain size distributions were statistically compared using the Hellinger distance to evaluate the similarity between two distributions. It was found that the orientation mapping-based method produced a somewhat different distribution compared with the hand-tracing method. It was argued that the difference is caused by the persistence of pseudosymmetry boundaries that cannot be removed in

an automated way using currently available clean-up procedures in the analysis software. If the mean grain size value is the only concern, then the automated orientation mapping-based grain size measurement method can be considered to be of high accuracy and efficiency for nanocrystalline materials.

## Acknowledgements

Financial support of the SRC Tasks 1292.008, 2121.001 and 2323.001, and of the MRSEC program of the NSF under DMR-0520425 is gratefully acknowledged. Prof. M. De Graef and Dr. P.G. Callahan are acknowledged for their suggestions about using the Hellinger distance. Dr. S.P. Donegan is acknowledged for his help in making probability plots.

## References

- [1] Sun T, Yao B, Warren AP, Barmak K, Toney MF, Peale RE, et al. *Phys Rev B* 2010;81:155454.
- [2] Lu L, Shen YF, Chen XH, Qian LH, Lu K. *Science* 2004;304:422–6.
- [3] Suzuki T, Kosacki I, Anderson HU. *Solid State Ionics* 2002;151:111–21.
- [4] Gianola D, Van Petegem S, Legros M, Brandstetter S, Van Swygenhoven H, Hemker K. *Acta Mater* 2006;54:2253–63.
- [5] Barmak K, Eggeling E, Kinderlehrer D, Sharp R, Ta'asan S, Rollett A, et al. *Prog Mater Sci* 2013;58:987–1055.
- [6] Backofen R, Barmak K, Elder K, Voigt A. *Acta Mater* 2014;64:72–7.
- [7] Rauch EF, Dupuy L. *Arch Metall Mater* 2005;50:87–99.
- [8] Rauch EF, Portillo J, Nicolopoulos S, Bultreys D, Rouvimov S, Moeck P. *Z Kristallogr* 2010;225:103–9.
- [9] Rouvimov S, Rauch EF, Moeck P, Nicolopoulos S. *Microsc Microanal* 2009;15:1290–1.
- [10] Vincent R, Midgley PA. *Ultramicroscopy* 1994;53:271–82.
- [11] Darbal AD, Ganesh KJ, Liu X, Lee SB, Ledonne J, Sun T, et al. *Microsc Microanal* 2013;19:111–9.
- [12] Liu X, Choi D, Beladi H, Nuhfer NT, Rohrer GS, Barmak K. *Scripta Mater* 2013;69:413–6.
- [13] Carpenter JS, Liu X, Darbal A, Nuhfer NT, McCabe RJ, Vogel SC, et al. *Scripta Mater* 2012;67:336–9.
- [14] Liu X, Nuhfer N, Rollett A, Sinha S, Lee S-B, Carpenter J, et al. *Acta Mater* 2014;64:333–44.
- [15] Liu X, Warren A, Nuhfer T, Rohrer G, Coffey K, Barmak K. *Microsc Microanal* 2013;19:1774–5.
- [16] Liu X, Nuhfer T, Ledonne J, Lee S, Rollett A, Barmak K, et al. *Microsc Microanal* 2012;18:1426–7.
- [17] Feltham P. *Acta Metall* 1957;5:97–105.
- [18] Raeisinha B, Sinclair C. *Mater Sci Eng A* 2009;525:78–82.
- [19] Bhattacharyya A. *Bull Calcutta Math Soc* 1943;35:4.
- [20] Callahan P, Simmons J, De Graef M. *Model. Simul. Mater Sci* 2013;21:015003.
- [21] Aherne FJ, Thacker NA, Rockett PI. *Kybernetika* 1998;34:363–8.
- [22] Donegan S, Tucker J, Rollett A, Barmak K, Groeber M. *Acta Mater* 2013;61:5595–604.
- [23] Tucker JC, Chan LH, Rohrer GS, Groeber MA, Rollett AD. *Metall Mater Trans A* 2012;43:2810–22.
- [24] Yao B, Petrova RV, Vanfleet RR, Coffey KR. *J Electron Microsc* 2006;55:209–14.
- [25] Rauch EF, Veron M. *Materialwiss Werkst* 2005;36:552–6.
- [26] Rauch ER, Duft A. *Textures Mater* 2005:197–202.
- [27] Moeck P, Rouvimov S, Rauch EF, Veron M, Kirmse H, Hausler I, et al. *Cryst Res Technol* 2011;46:589–606.
- [28] Gjonnes K. *Ultramicroscopy* 1997;69:1–11.
- [29] Carpenter DT, Rickman JM, Barmak K. *J Appl Phys* 1998;84:5843–54.